Effect of temperature on irreversible and reversible heat generation rates in ionic liquid-based electric double layer capacitors

Ampol Likitchatchawankun [a], Grace Whang [b], Jonathan Lau [b], Obaidallah Munteshari [a, c], Bruce Dunn [b], Laurent Pilon [a, *]

[a] Mechanical and Aerospace Engineering Department, Henry Samueli School of Engineering and Applied Science, University of California, Los Angeles, CA, 90095, USA
[b] Materials Science and Engineering Department, Henry Samueli School of Engineering and Applied Science, University of California, Los Angeles, CA, 90095, USA
[c] Mechanical Engineering Department, King Fahd University of Petroleum and Minerals (KFUPM), Dhahran, 31261, Saudi Arabia

ARTICLE INFO

ABSTRACT

This study reports for the first time, isothermal calorimetric measurements of the instantaneous heat generation rate at each electrode of ionic liquid-based electric double layer capacitors (EDLCs) at different temperatures. Indeed, EDLCs generate reversible and irreversible heat during normal operation and the properties of ionic liquids are known to depend strongly on temperature. Here, the EDLC cell consisted of two identical activated carbon electrodes separated by a mesh separator submerged in ionic liquid-based electrolyte consisting of 1 M N-butyl-n-methylpyrrolidinium bis(trifluoromethane sulfonyl) imide (Pyr$_{14}$TFSI) dissolved in propylene carbonate (PC). The instantaneous heat generation rate at each electrode was measured at 20 °C, 40 °C, and 60 °C under galvanostatic cycling using an *in operando* calorimeter. The potential window was limited to 1 V to compare with results from similar devices using aqueous or organic electrolytes. The time-averaged irreversible heat generation was attributed to Joule heating and decreased with increasing temperature due to the associated decrease in internal resistance. Furthermore, the reversible heat generation rates at the positive and negative electrodes were mostly exothermic during charging due to ion adsorption and endothermic during discharging due to ion desorption. They increased slightly with increasing temperature as a result of increasing charge storage. The reversible heat generation rate at the positive electrode was slightly larger than that at the negative electrode. In fact, an endothermic dip was observed in the reversible heat generation rate at the negative electrode at the beginning of charging caused by overscreening effect and/or desolvation of Pyr$_{14}^+$ cations as they enter the activated carbon pores.

© 2020 Elsevier Ltd. All rights reserved.

1. Introduction

Electric double layer capacitors (EDLCs) have drawn significant attention as electrical energy storage systems thanks to their large power densities, high cycle efficiency, and long cycle life compared with batteries [1–4]. EDLC devices consist typically of two carbon-based electrodes and a separator immersed in concentrated aqueous, organic, or ionic liquid electrolytes [5,6]. They store charges physically in the electric double layer (EDL) forming at the porous electrode/electrolyte interface [5–8]. They are promising for

electrical energy storage applications requiring charging/discharging at high rate such as the utility grid and regenerative braking in hybrid or electric vehicles [7–13]. In such high power applications, EDLCs can experience a significant amount of heat generation resulting in excessively high cell temperatures [12–15]. Elevated temperatures, in turn, can lead to (i) increased self-discharge rates [14–16], (ii) accelerated aging of the device [12–18], and (iii) electrolyte decomposition and evaporation [16,18,19]. On the other hand, depending on the electrolyte, increasing the device temperature can increase the ion mobility in the electrolyte leading to improved ionic conductivity and reduced electrolyte resistance and equivalent series resistance (ESR) of the device [20,21].

Ionic liquids (ILs) and their mixtures have been considered as

Nomenclature

A	Footprint area of the heat flux sensor, cm^2
$C_{diff,m}$	Gravimetric differential capacitance, F/g
$C_{int,m}$	Gravimetric integral capacitance, F/g
D	Diffusion coefficient, m^2/s
I	Current, mA
m	Mass loading of active material in electrode, mg
n_c	Cycle number
q''	Heat flux, mW/cm^2
$\dot{Q}$	Heat generation rate, mW
$\bar{\bar{Q}}$	Time-averaged heat generation rate, mW
R	Resistance, Ω
R_s	Internal resistance for entire device, Ω
S	Heat flux sensor sensitivity, $\mu V/(W/cm^2)$
t	Time, s
t_c^-	Time immediately after the beginning of the discharging step, s
t_c^+	Time at the end of the charging step, s
T	Temperature or absolute temperature, $°$C or K

ΔV	Voltage difference generated in the heat flux sensor, μV
z_i	Valency, -

Greek symbols

ν	Scan rate, mV/s
σ	Ionic conductivity, mS/cm
$\psi_{s,min}$	Minimum cell potential, V
$\psi_{s,max}$	Maximum cell potential, V
$\psi_s(t)$	Cell potential, V

Superscripts and subscripts

c	Refers to charging step
cd	Refers to charging-discharging cycle
d	Refers to discharging step
i	Refers to ion species "i"
J	Refers to Joule heating
T	Refers to entire cell
rev,i	Refers to reversible heat generation
$+$ or $-$	Refers to positive or negative electrode

electrolytes in EDLCs due to their thermal stability at high temperatures [22−27], their wide potential windows [25−30], and the ability to operate at low temperatures [23,26,30,31]. Note, however, that degradation may already occur at temperatures considerably lower than the onset temperature of decomposition. Thus, the maximum operating temperature must be adjusted accordingly [25]. Neat ILs typically suffer from low ionic conductivity ($\sim$ 1−20 mS/cm at room temperature) [22,24,32−36] compared with organic or aqueous electrolytes ($\sim$ 200−800 mS/cm) [35,36]. However, their ionic conductivity increases sharply with increasing temperature [22,37−40]. Another way to improve the ionic conductivity of ILs consists of dissolving them in nitrile-based or carbonate-based organic solvents such as acetonitrile (ACN), propylene carbonate (PC), and/or ethylene carbonate (EC)-dimethyl carbonate (DMC) mixtures [22,23,41]. The improvement in ionic conductivity and the decrease in viscosity are realized by reducing the ion pairing association of the neat ILs via solvation [23].

Heat generation in EDLCs under normal operating conditions can be attributed to (i) irreversible heat generation including Joule heating [1,42−44] and (ii) reversible heat generation due to ion diffusion, steric effects, and changes in the entropy of mixing of the electrolyte [14,44−47]. During charging, ions migrate to and adsorb onto the electrode/electrolyte interface to form an electric double layer (EDL). Thus, the electrolyte undergoes a process from a disordered state to an ordered state. Then, its entropy is reduced and, at constant temperature, thermal energy is released, i.e., the process is exothermic. By contrast, during discharging, ions redistribute into the bulk electrolyte, the electrolyte entropy increases and the process is endothermic.

The present study aims to assess, for the first time, the effect of operating temperature on the instantaneous heat generation rate in EDLCs consisting of two activated carbon electrodes separated by a mesh separator immersed in an ionic liquid-based electrolyte. The instantaneous heat generation rate at each electrode was measured in a recently developed *in operando* calorimeter [48] under galvanostatic cycling at 20 $°$C, 40 $°$C, and 60 $°$C. The results were analyzed in terms of reversible and irreversible heat generation rates and compared with similar measurements on EDLCs but with aqueous and organic electrolytes at 20 $°$C. They can provide insight into the physicochemical processes occurring during normal operation.

They can also be used in the design of thermal management solutions for EDLCs.

2. Background

2.1. Pyr$_{14}$TFSI ionic liquid electrolyte

Ionic liquid N-butyl-N-methylpyrrolidinium bis(trifluoromethane sulfonyl)imide (Pyr$_{14}$TFSI) and its mixtures with organic solvents has been used extensively as electrolytes in EDLCs due to exceptional cycling stability, thermal stability, and wide operating potential window [28,33,49−51]. The potential window of neat Pyr$_{14}$TFSI or of its mixture with PC can be as high as $\sim$ 3.5 V [31] compared with $\leq$ 3 V for organic electrolytes (e.g., acetonitrile) and $\sim$ 1 V for aqueous electrolytes [52]. Despite the fact that the onset temperature of decomposition of neat Pyr$_{14}$TFSI is about 350−385 $°$C [38,53], its temperature range of use is recommended from 20 to 60 $°$C [31]. In addition, Pyr$_{14}$TFSI-based electrolytes shows larger power and/or energy densities and also better capacitance retention compared to tetraethylammonium tetrafluoroborate (TEABF$_4$) in PC or ACN, as conventional organic electrolytes [28,54]. Furthermore, leakage current was about three times smaller in AC-based EDLCs with neat Pyr$_{14}$TFSI or Pyr$_{14}$TFSI in PC than with TEABF$_4$ in PC [55]. Here, ionic conductivity of neat Pyr$_{14}$TFSI is as low as $\sim$ 2.0 mS/cm at 20 $°$C [53,56], however, it depends strongly with temperature and increases to $\sim$ 7.0 mS/cm at 60 $°$C [50,57]. In addition, by mixing Pyr$_{14}$TFSI ionic liquid in PC (1:1 wt%), the electrolyte ionic conductivity increased from 2.6 to 10.3 mS/cm at 25 $°$C [28]. However, the potential window and the operating temperature may be further limited by the solvent decomposition [58].

2.2. Effect of temperature on EDLCs

Several studies have investigated the effect of temperature on the performance of EDLCs with various electrolytes [17−21,59−67]. Electrochemical measurement methods such as cyclic voltammetry (CV), galvanostatic charge/discharge cycling, and impedance spectroscopy (EIS) were performed within the temperature range of −40 $°$C−100 $°$C on (i) commercial EDLC devices and module

[17,20,21,60−62] and on (ii) scientific test cells in three-electrode setup [63] and two-electrode cells [19,20,59,67]. First, the cell internal resistance R_s was found to decrease with increasing temperature due to the associated increase in ion mobility in organic [17,19,62] as well as in ILs [20] electrolytes. For the same reason, the specific capacitance increased with increasing temperature [19,20,62,63,68] which was sometimes attributed to additional faradaic reactions [19,63].

Moreover, temperature can have a negative effect on the self-discharge rate of EDLCs [14−16]. Indeed, at high temperatures, ions possess higher mobility leading to higher desorption rates and self-discharge [17,67,69]. Furthermore, high operating temperatures and/or high applied voltages can lead to accelerated aging of EDLCs due to thermal and electrochemical degradation of the electrolyte and/or electrode materials [60,70]. Indeed, increasing the operating temperature resulted in increasing aging rate in some commercial EDLCs [18]. First, under high temperature, electrolyte may decompose to produce gases such as H_2, CO, and other organic byproducts [70]. Such gas production leads to excessive pressure rise inside the cell thus increasing the risks of explosion [71]. The gases generated can also obstruct access of the porous electrodes to the liquid electrolyte leading to a decrease in the device capacitance and/or an increase in its resistance [60,70]. Similarly, high temperature can promote accelerated decomposition reactions in the electrode and/or in the electrolyte by oxidation/reduction reactions resulting in solid byproducts [72]. These byproducts can adhere to the electrode/electrolyte interface thus reducing the electrode active surface area [72].

2.3. Heat generation in EDLC devices

2.3.1. Thermal modeling of EDLCs

Several thermal models have been proposed in the literature to predict the temperature evolution in EDLCs using numerical or analytical methods [13−16,44−47]. Many of these models solved the transient energy conservation equation with heat generation accounting only for Joule heating [13,15,16]. By contrast, Schiffer et al. [14] developed a thermal model for EDLCs including irreversible Joule heating and reversible heat generation due to changes in entropy of the electrolyte during EDL formation at the electrode/electrolyte interface (entropy of mixing), as explained previously. The reversible heat generation rate was modeled to be linearly proportional to the imposed current under galvanostatic cycling [14].

More recently, d'Entremont and Pilon [45] developed a first-order time-dependent thermal model for EDLCs based on the lumped-capacitance approximation and accounting for both irreversible Joule heating and reversible heat generation rates. The latter was also modeled as linearly proportional to the imposed current during galvanostatic cycling [45]. The temporal temperature evolution predicted was in good agreement with experimental data acquired from commercial EDLCs and reported in the literature [14−16]. Furthermore, the same authors developed a more refined physical model based on first principles by coupling (i) the modified Poisson-Nernst-Planck (MPNP) model with (ii) the energy conservation equation to derive expressions for both the irreversible and reversible heat generation rates in EDLCs with symmetric [46] or asymmetric [47] binary electrolytes for different ion diameters and diffusion coefficients. The two main contributions of heat generation rate in EDLCs arise from (i) ions decreasing their electrical potential energy and (ii) ion transport towards states of smaller entropy (heat of mixing) [47]. The former can be decomposed into three different contributions namely Joule heating, ion diffusion, and steric repulsion [47]. In addition, the heat of mixing arises from concentration and temperature gradients [47]. In all cases, the source of irreversible heat generation was exclusively Joule heating [46,47]. In addition, larger ion concentrations, diffusion coefficients and/or ion valencies led to smaller irreversible heat generation rate due to an increase in electrolyte electrical conductivity [47]. On the other hand, the instantaneous reversible heat generation was attributed to ion diffusion, steric effects, and entropy changes during charging and discharging [46,47]. It was found to be exothermic during charging and endothermic during discharging [46,47]. For binary asymmetric electrolytes, the reversible heat generation rate was different at the positive and negative electrodes [47]. In fact, the reversible heat generation rate at a given electrode increased with increasing valency and decreasing diameter of the counterion but was independent of ion diffusion coefficients [47].

2.3.2. Experimental calorimetry

Few experimental studies have investigated heat generation in EDLCs [44,48,73]. Dandeville et al.[44] developed an electrochemical calorimeter measuring time-dependent temperature variation in two-electrode cells under galvanostatic cycling. Here, the heat generation rate in the entire cell was calculated by deconvoluting the measured time-dependent cell temperature during cycling [44]. In addition, the heat generation rates at both electrodes in a AC-based EDLC cell were assumed to be identical and equal to half of that measured in the entire cell [44]. Furthermore, heat generation was decomposed into (i) irreversible heat generation caused by Joule heating and (ii) reversible heat generation caused by electric double layer (EDL) formation [44]. More recently, Munteshari et al. [48,73] developed an *in operando* calorimeter measuring the time-dependent irreversible and reversible heat generation rates at each electrode of supercapacitors. The authors investigated EDLC cells consisting of two identical AC-based electrodes immersed in different organic or aqueous liquid electrolytes under cycling at constant current I [48,73]. For all aqueous and organic electrolytes tested, the irreversible heat generation rate at each electrode was found to be proportional to I^2 under constant current cycling with a potential window of 1 V. The total irreversible heat generation in the cell was equal to Joule heating expressed as $\bar{Q}_J = R_s I^2$ where R_s is the internal resistance of the device measured from IR drop and found to be independent of current I [48]. Irreversible heat generation was the smallest in aqueous electrolytes as they typically have the largest ionic conductivity [35,36]. Furthermore, reversible heat generation rate at the positive electrode was (i) exothermic during charging due to ion adsorption and (ii) endothermic during discharging due to ion desorption, as predicted theoretically [46,47]. By contrast, at the negative electrode, the reversible heat generation rate was first endothermic and then exothermic during charging [48]. This was shown to be caused by negatively charged functional groups associated with carboxymethyl cellulose (CMC) binder forming at the negative electrode and responsible for the overscreening effect [73]. Indeed, the CMC binder consisted of carboxymethyl (− CH_2COONa) and hydroxyl (− OH) functional groups [73]. These groups dissociated in 1 M $LiPF_6$ in EC:DMC organic electrolyte forming negatively charged functional groups (− CH_2COO^-) and (− O^-) that attracted cations (e.g., Li^+), leading to overscreening of the electrode surface [73,74]. In order to balance the charge of the inner Helmholtz layer in the electrolyte, an additional layer of anions was required [73,74]. Therefore, the negative electrodes containing CMC was first charged by repelling this anion layer (endothermic) followed by cations adsorption (exothermic) [73,75].

Overall, previous calorimetric studies have investigated the instantaneous heat generation rate at constant temperature around 20 °C in EDLCs with aqueous or organic electrolytes [44,48,73]. To the best of our knowledge, neither heat generation in IL-based

EDLCs nor the effect of temperature on the irreversible and reversible heat generation rates in EDLCs have been investigated to date. In fact, ILs enable normal operation under a wide range of temperature and their properties are known to depend strongly on temperature. In addition, for ILs dissolved in organic solvents, solvated ions must be fully or partially desolvated in order to enter the pores and to form EDL at the electrode/electrolyte interface during charging [8,76]. Desolvation is an endothermic process since the enthalpy of solvation is always positive (exothermic) due to van der Waals forces controlling the interaction between the ions and the solvent molecules [36,77,78].

The present study aims to perform isothermal calorimetric measurements in IL-based EDLCs under galvanostatic cycling at temperature between 20 and 60 °C. The irreversible and reversible heat generation rates in EDLC cells made of AC-based electrodes with electrolyte consisting of 1 M Pyr$_{14}$TFSI in PC were investigated and compared with results from similar devices and potential window but using aqueous or organic electrolytes [48]. The results can also be used to develop thermal management strategies for EDLCs.

3. Materials and methods

3.1. Electrode and device fabrication

Activated carbon slurries were prepared by mixing activated carbon (YP−50F, Kuraray Chemical), TX-100 surfactant (DOW Chemical), carboxymethyl cellulose (CMC, DOW Chemical) as a thickening agent/binder, and styrene-butadiene rubber (SBR, MTI Corp.) as a binder, in DI water in an 80:5:1.5:13.5 wt ratio. The slurry was drop casted onto carbon-coated aluminum current collector sheets (MTI Corp.) with 1×1 cm^2 footprint area. The current collectors had been previously treated by oxygen plasma to enhance their hydrophilicity and ensure uniform spreading of the slurry. The electrodes were dried in a vacuum oven at 120 °C for 24 h before being placed in a glove box under argon (Ar) atmosphere (< 1 ppm H$_2$O/O$_2$). The mass loading on each electrode was 2.5 mg (2.0 mg of AC) corresponding to an electrode thickness of about 60 μm.

The EDLC cell consisted of two identical activated carbon electrodes separated by a 1 mm-thick chemical-resistant poly-propylene mesh separator with electrolyte made of 1 M Pyr$_{14}$TFSI ionic liquid electrolyte dissolved in PC. Here, PC was used to dilute the ionic liquid Pyr$_{14}$TFSI in order to increase the ionic conductivity of the electrolyte and improve the wetting of the AC electrodes without sacrificing thermal stability since the boiling temperature of PC is around 240 °C [23]. In addition, the concentration of 1 M Pyr$_{14}$TFSI in PC was selected in this experiment because it corresponds to the maximum ionic conductivity of about 8.3 mS/cm and its lowest viscosity around 5 mPa s at 20 °C [79]. Finally, the device was assembled and placed in the calorimeter compartment inside the glove box under Ar atmosphere before being taken out for isothermal calorimetric measurements at temperature between 20 °C and 60 °C.

3.2. Device characterization

The device's gravimetric integral capacitance $C_{int,m}$ (in F/g) was evaluated from cyclic voltammetry (CV) curve as a function of scan rate ν according to Ref. [80],

$$C_{int,m}(\nu) = \frac{1}{m(\psi_{s,max} - \psi_{s,min})} \oint \frac{I(\psi_s)}{2\nu} d\psi_s \tag{1}$$

where ν is the scan rate varying from 5 to 30 mV/s. Here, m is the

total mass loading of AC ($m = 4.0$ mg) in both electrodes while $I(\psi_s)$ is the measured current at cell potential ψ_s over the potential window ranging between $\psi_{s,min} = 0$ V and $\psi_{s,max} = 1$ V. This potential window may appear narrow for IL-based EDLCs but it was selected (i) to facilitate comparison with previous experimental studies measuring the heat generation rate at 20 °C in EDLCs using aqueous and organic electrolytes [48,73] and (ii) to avoid parasitic phenomena occurring under larger potential window range including potential ion intercalation in AC [81] and/or electro-chemical decomposition of solvent PC [58]. Subsequently, galva-nostatic cycling was performed on the device with constant current I ranging from 2 to 6 mA and at temperature of 20 °C, 40 °C, or 60 °C. Here, fifteen consecutive cycles were performed for each value of current I to ensure that oscillatory steady state had been reached in the calorimetric measurements. The gravimetric differential capacitance $C_{diff,m}$ (in F/g) can be estimated from galvano-static cycling according to Ref. [80],

$$C_{diff,m}(I) = \frac{I}{m|d\psi_s/dt|} \tag{2}$$

where $|d\psi_s/dt|$ was estimated for each cycle, at the end of the discharging and charging steps.

Furthermore, the internal resistance R_s was calculated from the IR drop at the charging/discharging transitions under galvanostatic cycling at current I [82−85],

$$R_s(I) = \frac{\psi_s(t_c^+) - \psi_s(t_c^-)}{2I} \tag{3}$$

where $\psi_s(t_c^+)$ and $\psi_s(t_c^-)$ denote the potentials across the cell at the end of the charging step and immediately after the beginning of the discharging step, respectively. The IR drop, $\psi_s(t_c^+) - \psi_s(t_c^-)$, was obtained by estimating the cell potential $\psi_s(t_c^-)$ 10 ms after the beginning of the discharging step (i.e., $t_c^+ - t_c^- = 10$ ms), as sug-gested for supercapacitors by Zhao et al. [83] and successfully used in our previous studies [48,73].

3.3. Isothermal calorimeter

In this study, the instantaneous heat generation rate at each electrode of the device was measured under galvanostatic cycling at constant temperature of 20 °C, 40 °C, and 60 °C using an *in operando* calorimeter described in Ref. [48]. According to the thermal analysis of a single electrode (see Supplementary Materials of Ref. [48]), the instantaneous heat generation rate $\dot{Q}_i(t)$ (in mW) at each electrode is equal to the heat transfer rate $q_i''(t)$ passing through the thermoelectric heat flux sensor placed in thermal contact with the current collector, such that [48],

$$\dot{Q}_i(t) = q_i''(t)A_i = \frac{\Delta V_i(t)}{S_i}A_i \quad \text{with } i = + \text{ or } - \tag{4}$$

where A_i refers to the footprint area of the electrode (in cm^2) and S_i denotes the temperature-dependent sensitivity of the heat flux sensor provided by the manufacturer (in μV/(W/m^2)). Here, subscript "i" refers to either the positive " + " or negative " − " electrode. In addition, $\Delta V_i(t)$ refers to the voltage difference measured within each thermoelectric heat flux sensor in thermal contact with electrode "i". The instantaneous total heat generation rate in the entire device (denoted by subscript "T") can be written as $\dot{Q}_T(t) = \dot{Q}_+(t) + \dot{Q}_-(t)$.

In addition, the instantaneous heat generation rate $\dot{Q}_i(t)$ in each electrode can be decomposed as the sum of the irreversible $\dot{Q}_{irr,i}(t)$ and reversible $\dot{Q}_{rev,i}(t)$ heat generation rates, i.e., $\dot{Q}_i(t) = \dot{Q}_{irr,i}(t) +$

$\dot{Q}_{rev,i}(t)$ [48,73]. By definition, time-averaging of the reversible heat generation rate $\dot{Q}_{rev,i}(t)$ at electrode "i" over a complete charging-discharging cycle yields $\overline{\dot{Q}}_{rev,i} = 0$. Therefore, the time-averaged heat generation rate $\dot{Q}_i(t)$ over a cycle period t_{cd} is equal to the time-averaged irreversible heat generation rate $\overline{\dot{Q}}_{irr,i}$ at electrode "i", i.e. [48,73],

$$\overline{\dot{Q}}_{irr,i} = \frac{1}{t_{cd}} \int_{(n_c-1)t_{cd}}^{n_c t_{cd}} \dot{Q}_i(t)\, dt \qquad \text{with } i = + \text{ or } -. \tag{5}$$

Here, n_c is the cycle number, chosen to be sufficiently large for $\dot{Q}_i(t)$ to reach oscillatory steady state. Finally, in the interest of comparing the reversible heat generation rate at each electrode, the instantaneous reversible heat generation rate $\dot{Q}_{rev,i}(t)$ was time-averaged solely over a charging period t_c according to Refs. [48,73],

$$\overline{\dot{Q}}^c_{rev,i} = \frac{1}{t_c} \int_{(n_c-1)t_{cd}}^{(n_c-1)t_{cd}+t_c} \dot{Q}_{rev,i}(t)\, dt \qquad \text{with } i = T, +, \text{ or } -. \tag{6}$$

4. Results and discussion

4.1. Cyclic voltammetry and gravimetric integral capacitance

Fig. 1(a) shows the measured CV curves of the device at 20 °C for five different scan rates ν between 5 and 30 mV/s. All curves featured a nearly rectangular and symmetrical shape characteristic of ideal EDLCs. Fig. 1(b) shows CV curves of the device at different temperatures for scan rate $\nu = 20$ mV/s. Here, the CV curves were also rectangular at all temperatures and expanded slightly from 20 to 60 °C. This was likely due to the increase in electrical conductivity of the electrolyte with increasing temperature, as previously discussed. Similar results were observed at all scan rates (see Supplementary Materials).

Fig. 2 plots the gravimetric integral capacitance $C_{int,m}$ of the device investigated [Equation (1)] as a function of scan rate ν for the three different temperatures. Here, $C_{int,m}$ was around 15−25 F/g, a typical value for carbon-based electrodes with organic or IL-based electrolytes for the range of scan rate considered [73,86−88]. Fig. 2 also indicates that the gravimetric integral capacitance $C_{int,m}$ decreased slightly with increasing scan rate ν for all three temperatures, as generally observed in various AC-based [48,89,90] and graphene-based [86] EDLCs. This can be attributed to ion-diffusion limitations in the porous electrodes [91]. Finally, Fig. 2 establishes that the gravimetric integral capacitance $C_{int,m}$ increased with increasing temperature for any given scan rate. For example, $C_{int,m}$ at $\nu = 20$ mV/s was 17 F/g at 20 °C and 21 F/g at 60 °C. This was due to better ion mobility at higher temperature.

4.2. Galvanostatic cycling

Fig. 3(a) shows galvanostatic charge-discharge curves plotting the cell potential $\psi_s(t)$ as a function of time t at 20 °C for five different values of imposed current I ranging from 2 to 6 mA. The cell potential $\psi_s(t)$ varied almost linearly with time t between the minimum $\psi_{s,min}$ and maximum $\psi_{s,max}$ potentials, except for the IR drop. These results confirm the near ideal EDLC behavior of the device also observed in CV curves. Fig. 3(a) indicates that as expected the IR drop $\psi_s(t_c^+) - \psi_s(t_c^-)$ increased with increasing current I [48,73,92]. In addition, Fig. 3(b) shows the galvanostatic charge-discharge curves obtained at current $I = 4$ mA for different temperatures. Here, the IR drop was the largest at 20 °C and
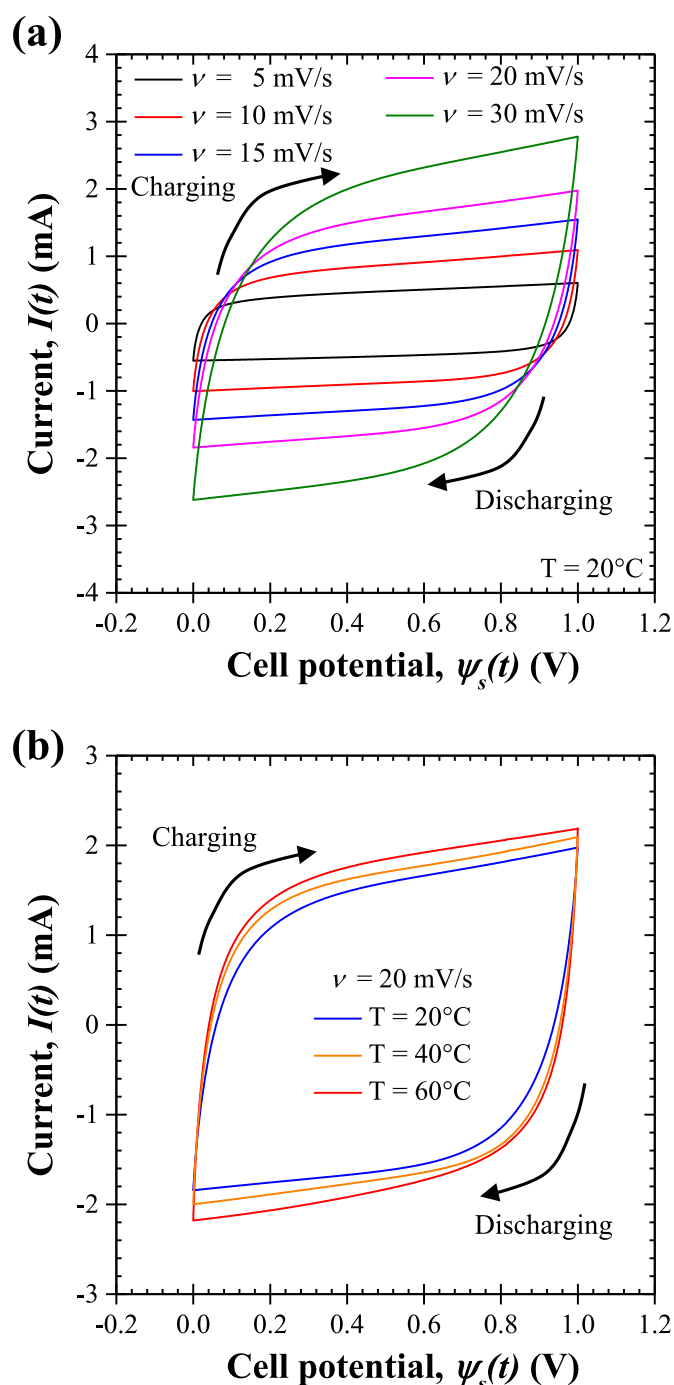

Fig. 1. Cyclic voltammogram from a two AC-electrode cell with 1 M Pyr$_{14}$TFSI in PC electrolyte (a) at 20 °C for scan rates ν between 5 and 30 mV/s, and (b) for scan rate $\nu = 20$ mV/s at temperature between 20 °C and 60 °C.

decreased with increasing temperature. This was due to the increasing electrolyte ionic conductivity with increasing temperature. In addition, the charging-discharging time t_{cd} increased with increasing temperature from 25 s at 20 °C to 34 s at 60 °C, as also observed in Refs. [19,20,63,68]. This increase in capacitance can be attributed to (i) the decrease in the electrolyte viscosity resulting in better infiltration of the electrolyte in the porous electrode [34,93,94] and to (ii) the increase in ion mobility in the electrolyte [19,20,62,63,68]. Similar results were obtained for different currents (see Supplementary Materials).
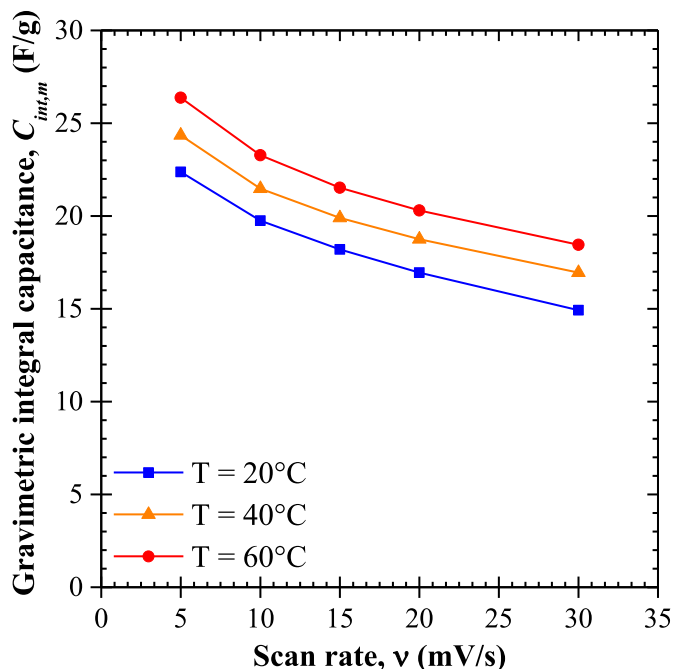
Fig. 2. Gravimetric integral capacitance $C_{int,m}$ obtained from CV curves of an AC-based EDLC cell with 1 M Pyr$_{14}$TFSI in PC electrolyte for three different temperatures 20 °C, 40 °C, and 60 °C for scan rate ν between 5 and 30 mV/s.

Fig. 4(a) shows the internal resistance R_s obtained from the IR drop [Equation (3)] as a function of galvanostatic cycle number n_c. Here, R_s was plotted for fifteen galvanostatic cycles at 20 °C, 40 °C, and 60 °C for each value of current I ranging from 2 to 6 mA. Here, the internal resistance R_s was fairly constant throughout $5 \times 15 = 75$ cycles for each temperature considered. In addition, Fig. 4(b) shows the average internal resistance $\overline{R}_s$ as a function of imposed current I for 20 °C, 40 °C, and 60 °C. Here, the average internal resistance $\overline{R}_s$ was relatively constant and independent of imposed current I. It is evident that both R_s and $\overline{R}_s$ decreased with increasing temperature from around $\overline{R}_s = 26.0 \pm 0.3$ Ω at 20 °C down to 17.9 ± 0.2 Ω at 40 °C, and 13.8 ± 0.2 Ω at 60 °C due to enhanced ions mobility.

Fig. 5(a) shows the gravimetric differential capacitance $C_{diff,m}$ as a function of galvanostatic cycle number n_c calculated by Equation (2). Here, $C_{diff,m}$ was plotted for fifteen cycles at 20 °C, 40 °C, and 60 °C for five different values of imposed current ranging from 2 to 6 mA. First, Fig. 5(a) indicates that $C_{diff,m}$ decreased with increasing current I. This could be due to ion diffusion limitation through the porous electrode under high current and fast charging time. In addition, $C_{diff,m}$ increased with increasing temperature for any given current I. For example, for $I = 4$ mA, $C_{diff,m}$ was 15.0 F/g at 20°C and increased by 15% and 24% at 40 °C and 60 °C, respectively. Furthermore, $C_{diff,m}$ was only slightly larger during charging than during discharging for any current imposed I and at any temperature, suggesting high energy efficiency. In fact, Fig. 5(b) shows the coulombic efficiency defined as the ratio of the discharging time t_d to the charging time t_c, i.e., $CE = t_d/t_c$ where t_c and t_d are the duration of the charging and discharging steps, respectively (Fig. 3). Here, CE was about 98% for the first cycle at each current I and reached nearly 100% in subsequent cycles indicating highly reversible capacity and good stability of the device even at 60 °C.

4.3. Instantaneous and time-averaged heat generation rates

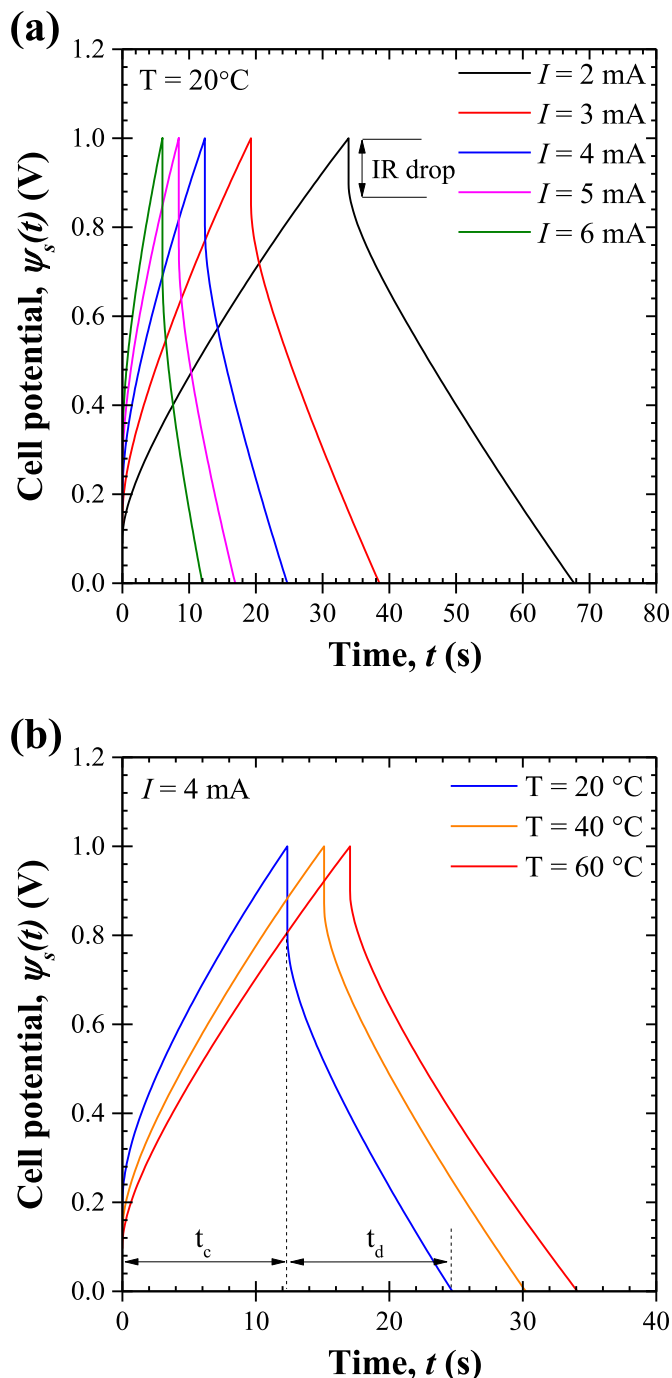Fig. 6(a)−(c) show the temporal evolution of the heat generation

Fig. 3. Cell potential under galvanostatic cycling (a) at 20 °C under imposed current I ranging between 2 and 6 mA, and (b) under imposed current $I = 4$ mA at 20 °C, 40 °C, and 60 °C.

rates $\dot{Q}_+(t)$ and $\dot{Q}_-(t)$ measured at the positive and negative electrodes and $\dot{Q}_T(t) = \dot{Q}_+(t) + \dot{Q}_-(t)$ as functions of dimensionless time t/t_{cd} for five consecutive galvanostatic cycles under constant current $I = 4$ mA and constant temperature of (a) 20 °C, (b) 40 °C, and (c) 60 °C. The corresponding time-averaged heat generation rates $\overline{\dot{Q}}_{irr,+}$, $\overline{\dot{Q}}_{irr,-}$, and $\overline{\dot{Q}}_{irr,T}$ are also shown. The results indicate that the heat generation rates, for all temperatures considered, were repeatable cycle after cycle. The heat generation rate at the negative electrode $\dot{Q}_-(t)$ oscillated with smaller amplitude than that at the positive electrode $\dot{Q}_+(t)$ at 20 °C. This difference
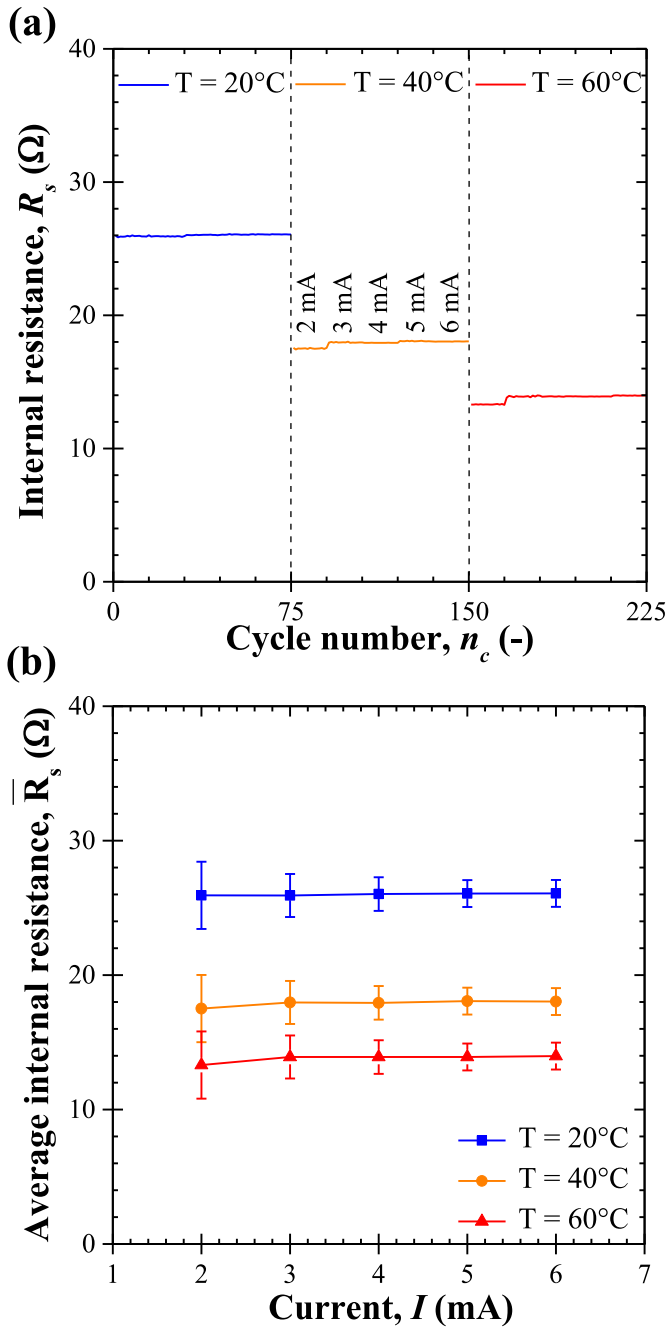
(a)

(b)

Fig. 4. (a) Internal resistance R_s of the IL-based EDLC cell investigated and retrieved from galvanostatic cycling at three different temperatures 20 °C, 40 °C, and 60 °C and under imposed current I ranging from 2 to 6 mA. (b) Average internal resistance $\overline{R}_s$ as a function of imposed current I at 20 °C, 40 °C, and 60 °C.
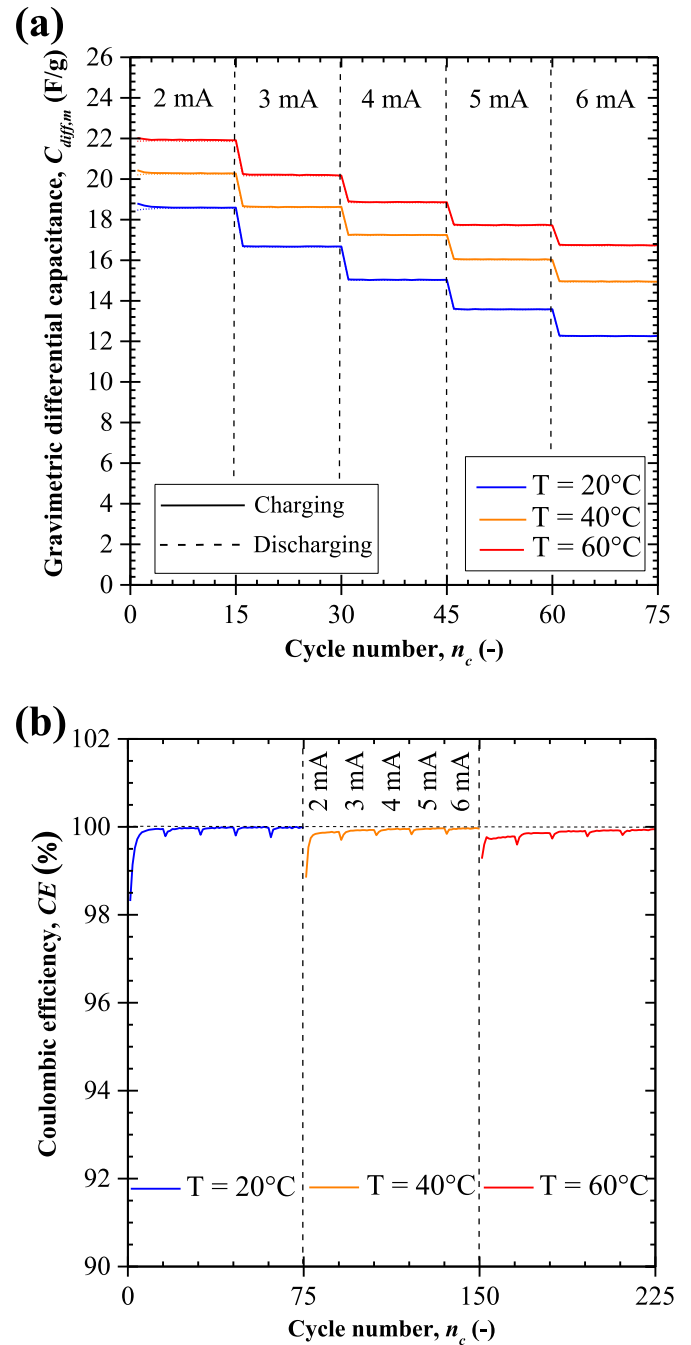
(a)

(b)

Fig. 5. (a) Gravimetric differential capacitance $C_{diff,m}$ of the IL-based EDLC cell investigated as a function of constant current cycle number during the charging and discharging steps and (b) coulombic efficiency CE for consecutive cycles at temperatures 20 °C, 40 °C, and 60 °C and for current I ranging from 2 to 6 mA.

between electrodes, however, vanished at 60 °C, as explained when considering the reversible heat generation rate at each electrode. In addition, the amplitude of oscillations in both $\dot{Q}_+(t)$ and $\dot{Q}_-(t)$ increased with increasing temperature, as discussed later.

Fig. 6(d)−(f) show the corresponding time-averaged irreversible heat generation rates $\overline{\dot{Q}}_{irr,+}$, $\overline{\dot{Q}}_{irr,-}$, and $\overline{\dot{Q}}_{irr,T}$ [Equation (5)] under galvanostatic cycling as functions of I^2 for constant current I ranging from 2 to 6 mA at (d) 20 °C, (e) 40 °C, and (f) 60 °C. The error bars correspond to two standard deviations or 95% confidence

interval estimated by evaluating $\overline{\dot{Q}}_{irr,i}$ for five consecutive cycles. Fig. 6(d)−(f) also show predictions for the heat generation rate due to Joule heating expressed as $\overline{\dot{Q}}_J = \overline{R}_s(T)I^2$ where $\overline{R}_s(T)$ is the average internal resistance reported in Fig. 4(b). These results established that the measured total irreversible heat generation rate $\overline{\dot{Q}}_{irr,T}$ under galvanostatic cycling was in excellent agreement with predictions of Joule heating $\overline{\dot{Q}}_J$ for all three temperatures considered. In other words, Joule heating was the main cause of irreversible heat generation in the EDLC cell investigated, for the
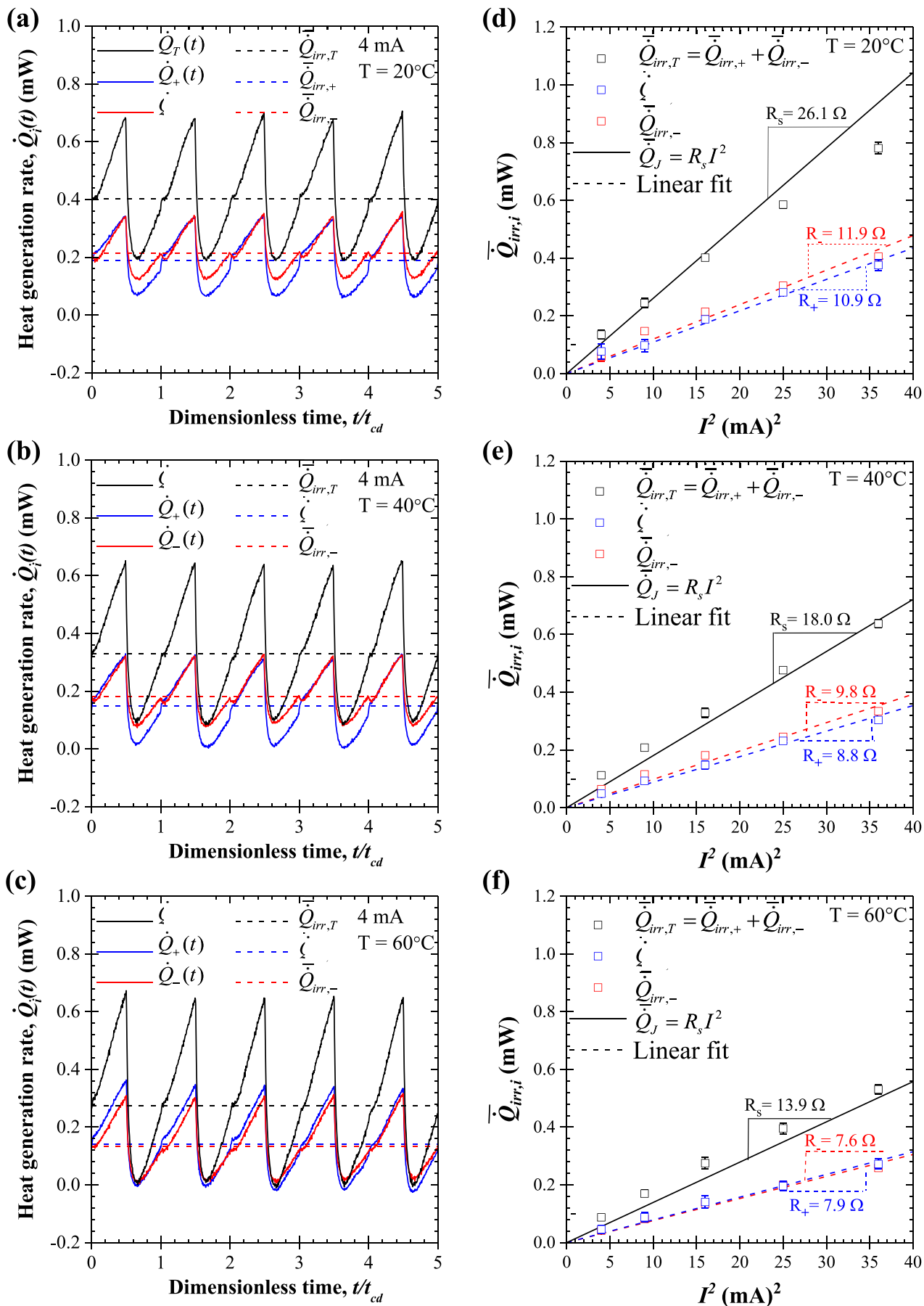
Fig. 6. Instantaneous heat generation rates $\dot{Q}_+(t)$ at the positive electrode, $\dot{Q}_-(t)$ at the negative electrode, and $\dot{Q}_T(t)$ in the entire cell as functions of the dimensionless time t/t_{cd} for current $I = 4$ mA at constant temperature of (a) 20 °C, (b) 40 °C, and (c) 60 °C. Time-averaged heat generation rates $\bar{\dot{Q}}_{irr,+}$, $\bar{\dot{Q}}_{irr,-}$, and $\bar{\dot{Q}}_{irr,T}$ under galvanostatic cycling as functions of I^2 for current I ranging between 2 and 6 mA at (d) 20 °C, (e) 40 °C, and (f) 60 °C.

potential window of 1 V. Similar results were obtained previously with EDLCs consisting of AC-based electrodes with aqueous or organic electrolytes under the same cycling conditions as in the present study [48,73].

Furthermore, for all temperatures, the time-averaged irreversible heat generation rates $\bar{\dot{Q}}_{irr,-}$ and $\bar{\dot{Q}}_{irr,+}$ at the negative and positive half-cells were linearly proportional to I^2 and the coefficient of proportionality corresponded to their respective resistances R_- and R_+. It is interesting to note that, at all temperatures, R_- and R_+ were very similar and that their sum was equal to the internal resistance R_s, i.e., $R_- \approx R_+$ and $R_- + R_+ \approx R_s$. Here, each half-cell resistance R_+ and R_- can be considered as the resistance of the electrode and electrolyte in series. First, the positive and negative electrodes were synthesized in the same manner and should be nearly identical. Second, the diffusion coefficients of Pyr$_{14}^+$ cations and TFSI$^-$ anions were similar when 1 M of Pyr$_{14}$TFSI is dissolved in PC, i.e., $D_+ \approx D_-$ [57,95]. Therefore, the ionic conductivities of the electrolyte in each half cell should also be similar, as observed in Fig. 6, for all temperatures. Finally, Fig. 6 establishes that both R_+ and R_- decreased with increasing temperature due to the corresponding increase in ion mobility [23].

4.4. Reversible heat generation rates

Joule heating was shown previously to dominate irreversible heat generation in EDLCs (Fig. 6). Thus, under constant current cycling, the instantaneous irreversible heat generation rate was independent of time, i.e., $\dot{Q}_{irr,i}(t) = \bar{\dot{Q}}_{irr,i} = R_i I^2$. Then, the instantaneous reversible heat generation rate $\dot{Q}_{rev,i}(t)$ at electrode "i" can be estimated by subtracting the irreversible heat generation rate $\bar{\dot{Q}}_{irr,i}$ from the instantaneous heat generation rate $\dot{Q}_i(t)$ to yield [48,73],

$$\dot{Q}_{rev,i}(t) = \dot{Q}_i(t) - \bar{\dot{Q}}_{irr,i} \qquad \text{with } i = + \text{ or } -. \tag{7}$$

Fig. 7 plots the instantaneous reversible heat generation rates (a) $\dot{Q}_{rev,+}(t)$ at the positive electrode, (b) $\dot{Q}_{rev,-}(t)$ at the negative electrode, and (c) $\dot{Q}_{rev,T}(t)$ in the entire cell as functions of the dimensionless time t/t_{cd} for current $I = 4$ mA at constant temperature of 20 °C, 40 °C, and 60 °C under oscillatory steady state. Here, two different cycles were plotted for each temperature, namely cycle number $n_c = 11$ and 15. Fig. 7(a)–(c) establish that $\dot{Q}_{rev,+}(t)$, $\dot{Q}_{rev,-}(t)$, and $\dot{Q}_{rev,T}(t)$ were repeatable from cycle to cycle and featured a similar behavior for all temperatures considered. In addition, the magnitude of the reversible heat generation rates $\dot{Q}_{rev,+}(t)$, $\dot{Q}_{rev,-}(t)$, and $\dot{Q}_{rev,T}(t)$ increased slightly with temperature. The same observations were made for different currents (see Supplementary Materials). This could be due to the fact that a larger number of ions were adsorbed at the electrode/electrolyte interface at higher temperature, as suggested by the larger capacitance [Fig. 5(a)]. Moreover, $\dot{Q}_{rev,+}(t)$ was slightly larger than $\dot{Q}_{rev,-}(t)$ for any value of temperature and current considered. Based on our previous first principle thermal model [47], this could be attributed to the fact that smaller TFSI$^-$ anions (~ 0.7 nm) were adsorbed at the positive electrode during charging thus generating more heat than adsorption of larger Pyr$_{14}^+$ cations (~ 1.1 nm) [57,79]. In addition, the difference between $\dot{Q}_{rev,+}(t)$ and $\dot{Q}_{rev,-}(t)$ became smaller as temperature increased. This could be due to the fact that higher temperatures (i) facilitate the desolvation of large and solvated Pyr$_{14}^+$ cations and (ii) accelerate the desorption process of sub-layer anions in overscreening effect at the negative electrode due to better ion mobility. The reversible heat generation rates $\dot{Q}_{rev,+}(t)$ and $\dot{Q}_{rev,-}(t)$ at the positive and negative electrodes were both mostly (i) exothermic during charging due to ion adsorption and (ii) endothermic during discharging due to ion desorption. This was

also consistent with results from numerical simulations [46,47]. Note that, $\dot{Q}_{rev,-}(t)$ featured a small endothermic dip at the beginning of the charging step that was not observed in $\dot{Q}_{rev,+}(t)$. This could be attributed to overscreening effect due to negatively charged functional groups of CMC binder, as observed also with organic and aqueous electrolytes [73]. Alternatively, it could be due to complete or partial endothermic desolvation of Pyr$_{14}^+$ cations of their PC solvation shell while moving into the AC pores to form an EDL during charging [8,36,76]. In fact, PC molecules are more likely to interact with Pyr$_{14}^+$ cations forming solvated PC − Pyr$_{14}^+$ cations [96] while TFSI$^-$ anions were found not to be significantly solvated by PC [97].

Finally, Fig. 7 shows the time-averaged reversible heat generation rates during a charging step (d) $\bar{\dot{Q}}_{rev,+}^c$ at the positive electrode, (e) $\bar{\dot{Q}}_{rev,-}^c$ at the negative electrode, and (f) $\bar{\dot{Q}}_{rev,T}^c$ in the entire cell as functions of current I ranging from 2 to 6 mA for temperature T of 20 °C, 40 °C, and 60 °C. It indicates that $\bar{\dot{Q}}_{rev,+}^c$, $\bar{\dot{Q}}_{rev,-}^c$, and $\bar{\dot{Q}}_{rev,T}^c$ increased slightly with increasing temperature while $\bar{\dot{Q}}_{rev,+}^c$ was larger than $\bar{\dot{Q}}_{rev,-}^c$ for any given current I, as expected from analyzing Fig. 7(a)-7(c). In addition, $\bar{\dot{Q}}_{rev,+}^c$, $\bar{\dot{Q}}_{rev,-}^c$, and $\bar{\dot{Q}}_{rev,T}^c$ increased linearly with imposed current I for all temperatures considered. This was consistent with previous experimental results for EDLC cells consisting of AC-electrodes with organic or aqueous electrolytes [44,48,73] and with numerical simulations of EDLCs [46].

During operation of commercial EDLCs, heat generation can result in significant temperature rise [12−16]. Thus, thermal management measures should be taken to prevent overheating. To do so, several strategies have been proposed including heat removal from EDLC modules by forced convection air-cooling [16], by circulating coolant, and by using phase change material [98]. The results of the present study could facilitate (i) the definition of safe modes of operation, (ii) the development of effective thermal management strategies, and (iii) the improvement of existing thermal model predicting the temperature evolution during operation.

5. Conclusion

This study measured, for the first time, the effects of operating temperature and the use of ionic liquid in organic solvent on the irreversible and reversible heat generation rates at each electrode of AC-based EDLCs. The electrolyte was 1 M Pyr$_{14}$TFSI in PC and the temperature varied between 20 and 60 °C while the potential window was limited to 1 V to facilitate comparison with previous studies on similar devices but using aqueous or organic electrolytes. The results establish that Joule heating was the main source of irreversible heat generation for the operating conditions considered. Similar results have been obtained previously with aqueous or organic electrolytes for similar devices and operating conditions at 20 °C. The internal resistance R_s and, consequently, the irreversible heat generation rate decreased with increasing temperature due to enhanced ion mobility in the IL-based electrolyte. In addition, the irreversible heat generation rates at the positive and negative electrodes were similar. Furthermore reversible heat generation rates at the positive and negative electrodes were mostly exothermic during charging and endothermic during discharging due to the change in entropy of the electrolyte system. It increased slightly with increasing temperature and was larger at the positive electrode due to the fact that adsorbing TFSI$^-$ anions were smaller than Pyr$_{14}^+$ cations. The reversible heat generation rate at the negative electrode featured a small endothermic dip at the beginning of the charging step potentially due to overscreening effect and/or endothermic desolvation of PC molecules from Pyr$_{14}^+$ cations.
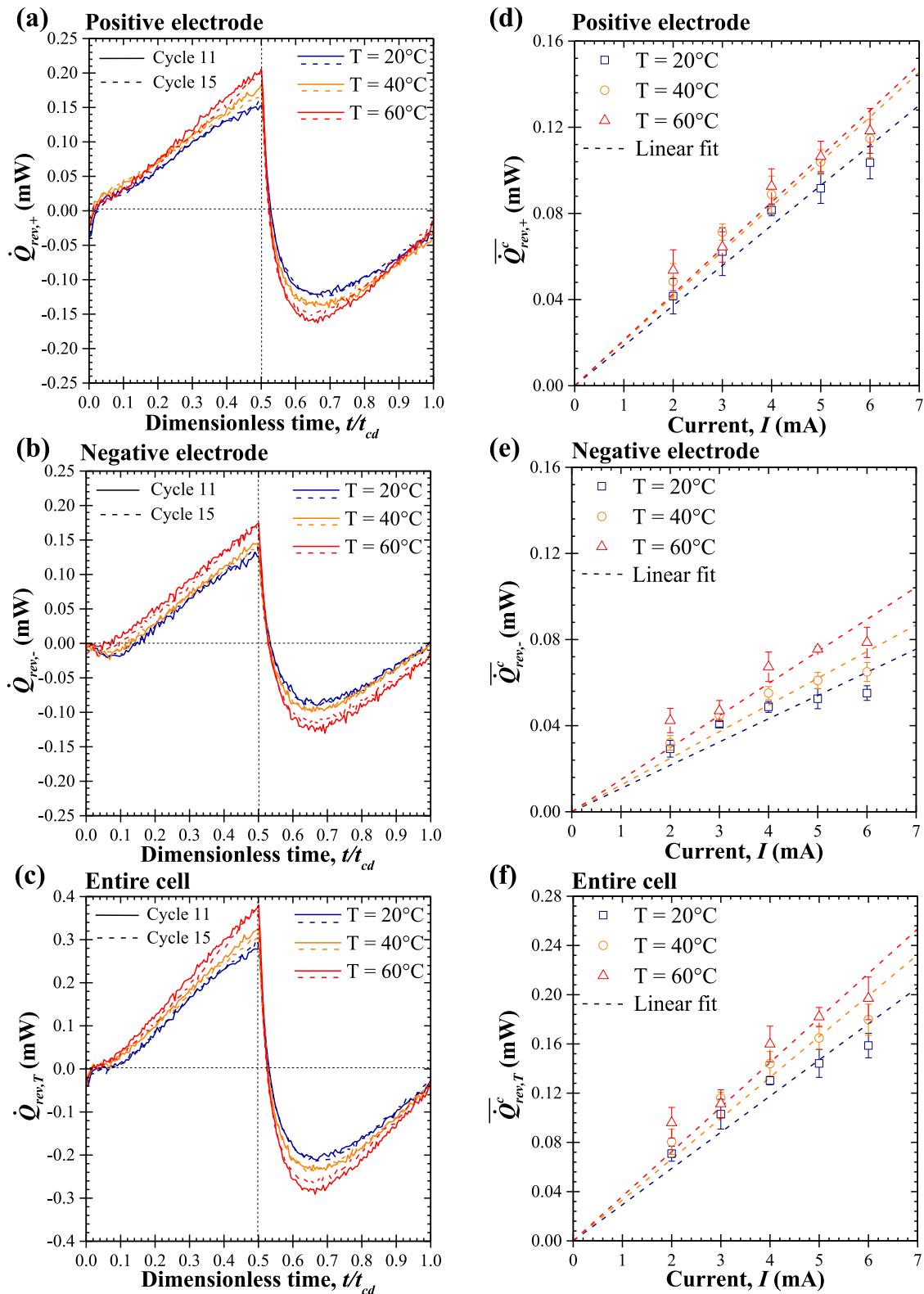
Fig. 7. Reversible heat generation rates (a) $\dot{Q}_{rev,+}(t)$ at the positive electrode, (b) $\dot{Q}_{rev,-}(t)$ at the negative electrode, and (c) $\dot{Q}_{rev,T}(t)$ in the entire cell as functions of the dimensionless time t/t_{cd} for two galvanostatic cycles under current $I = 4$ mA for temperature of 20 °C, 40 °C, and 60 °C. Time-averaged reversible heat generation rates during the charging step (d) $\overline{\dot{Q}}^{c}_{rev,+}$ at the positive electrode, (e) $\overline{\dot{Q}}^{c}_{rev,-}$ at the negative electrode, and (f) $\overline{\dot{Q}}^{c}_{rev,T}$ in the entire cell as functions of current I ranging between 2 and 6 mA for temperature of 20 °C, 40 °C, and 60 °C.

Acknowledgements

Appendix A. Supplementary data

Supplementary data to this article can be found online at https://doi.org/10.1016/j.electacta.2020.135802.

References

[1] B.E. Conway, Electrochemical Supercapacitors: Scientific Fundamentals and Technological Applications, Kluwer Academic/Plenum Publishers, New York, NY, 1999.

[2] J.B. Goodenough, H.D. Abruna, M.V. Buchanan, Basic research needs for electrical energy storage: report of the basic energy sciences workshop for electrical energy storage, april 2-4, 2007, Tech. Rep. (2007), https://doi.org/10.2172/935429. U.S. Department of Energy.

[3] A. Burke, R&D considerations for the performance and application of electrochemical capacitors, Electrochim. Acta 53 (3) (2007) 1083–1091.

[4] M. Winter, R.J. Brodd, What are batteries, fuel cells, and supercapacitors? Chem. Rev. 104 (2004) 4245–4270.

[5] L.L. Zhang, Y. Gu, X. Zhao, Advanced porous carbon electrodes for electrochemical capacitors, J. Mater. Chem. 1 (33) (2013) 9395–9408.

[6] F. Stoeckli, T.A. Centeno, Optimization of the characterization of porous carbons for supercapacitors, J. Mater. Chem. 1 (23) (2013) 6865–6873.

[7] P. Simon, Y. Gogotsi, Materials for electrochemical capacitors, Nat. Mater. 7 (11) (2008) 845–854.

[8] F. Béguin, V. Presser, A. Balducci, E. Frackowiak, Carbons and electrolytes for advanced supercapacitors, Adv. Mater. 26 (14) (2014) 2219–2251.

[9] L. Maharjan, S. Inoue, H. Akagi, A transformerless energy storage system based on a cascade multilevel PWM converter with star configuration, IEEE Trans. Ind. Appl. 44 (5) (2008) 1621–1630.

[10] A. Burke, Ultracapacitors: why, how, and where is the technology, J. Power Sources 91 (1) (2000) 37–50.

[11] M.D. Stoller, S. Park, Y. Zhu, J. An, R.S. Ruoff, Graphene-based ultracapacitors, Nano Lett. 8 (10) (2008) 3498–3502.

[12] J.R. Miller, Electrochemical capacitor thermal management issues at high-rate cycling, Electrochim. Acta 52 (4) (2006) 1703–1708.

[13] P. Guillemet, Y. Scudeller, T. Brousse, Multi-level reduced-order thermal modeling of electrochemical capacitors, J. Power Sources 157 (1) (2006) 630–640.

[14] J. Schiffer, D. Linzen, D.U. Sauer, Heat generation in double layer capacitors, J. Power Sources 160 (1) (2006) 765–772.

[15] H. Gualous, H. Louahlia-Gualous, R. Gallay, A. Miraoui, Supercapacitor thermal modeling and characterization in transient state for industrial applications, IEEE Trans. Ind. Appl. 45 (3) (2009) 1035–1044.

[16] M. Al Sakka, H. Gualous, J. Van Mierlo, H. Culcu, Thermal modeling and heat management of supercapacitor modules for vehicle applications, J. Power Sources 194 (2) (2009) 581–587.

[17] R. Kötz, M. Hahn, R. Gallay, Temperature behavior and impedance fundamentals of supercapacitors, J. Power Sources 154 (2) (2006) 550–555.

[18] O. Bohlen, J. Kowal, D.U. Sauer, Ageing behaviour of electrochemical double layer capacitors: Part I. experimental study and ageing model, J. Power Sources 172 (1) (2007) 468–475.

[19] C. Masarapu, H.F. Zeng, K.H. Hung, B. Wei, Effect of temperature on the capacitance of carbon nanotube supercapacitors, ACS Nano 3 (8) (2009) 2199–2206.

[20] S.I. Fletcher, F.B. Sillars, R.C. Carter, A.J. Cruden, M. Mirzaeian, N.E. Hudson, J.A. Parkinson, P.J. Hall, The effects of temperature on the performance of electrochemical double layer capacitors, J. Power Sources 195 (21) (2010) 7484–7488.

[21] H. Michel, Temperature and dynamics problems of ultracapacitors in stationary and mobile applications, J. Power Sources 154 (2) (2006) 556–560.

[22] M. Galiński, A. Lewandowski, I. Stepniak, Ionic liquids as electrolytes, Electrochim. Acta 51 (26) (2006) 5567–5580.

[23] V. Ruiz, T. Huynh, S.R. Sivakkumar, A.G. Pandolfo, "Ionic liquid–solvent mixtures as supercapacitor electrolytes for extreme temperature operation", RSC Adv. 2 (13) (2012) 5591–5598.

[24] C. Chiappe, D. Pieraccini, Ionic liquids: solvent properties and organic reactivity, J. Phys. Org. Chem. 18 (4) (2005) 275–297.

[25] C. Maton, N. De Vos, C.V. Stevens, Ionic liquid thermal stabilities: decomposition mechanisms and analysis tools, Chem. Soc. Rev. 42 (13) (2013) 5963–5977.

[26] M. Salanne, Chapter 2: ionic liquids for supercapacitor applications, in: B. Kirchner, E. Perlt (Eds.), Ionic Liquids II, Springer International Publishing, Cham, Switzerland, 2018, pp. 29–53.

[27] R. Hagiwara, J.S. Lee, Ionic liquids for electrochemical devices, Electrochemistry 75 (1) (2007) 23–34.

[28] A. Krause, A. Balducci, High voltage electrochemical double layer capacitor containing mixtures of ionic liquids and organic carbonate as electrolytes, Electrochem. Commun. 13 (8) (2011) 814–817.

[29] S. Pohlmann, A. Balducci, A new conducting salt for high voltage propylene carbonate-based electrochemical double layer capacitors, Electrochim. Acta 110 (2013) 221–227.

[30] R. Lin, P.-L. Taberna, S. Fantini, V. Presser, C.R. Pérez, F. Malbosc, N.L. Rupesinghe, K.B.K. Teo, Y. Gogotsi, P. Simon, Capacitive energy storage from- 50 to 100 °C using an ionic liquid electrolyte, J. Phys. Chem. Lett. 2 (19) (2011) 2396–2401.

[31] A. Balducci, Electrolytes for high voltage electrochemical double layer capacitors: a perspective article, J. Power Sources 326 (2016) 534–540.

[32] W. Xu, C.A. Angell, Solvent-free electrolytes with aqueous solution-like conductivities, Science 302 (5644) (2003) 422–425.

[33] S. Pohlmann, B. Lobato, T.A. Centeno, A. Balducci, The influence of pore size and surface area of activated carbons on the performance of ionic liquid based supercapacitors, Phys. Chem. Chem. Phys. 15 (40) (2013) 17287–17294.

[34] G. Xiong, A. Kundu, T.S. Fisher, Thermal Effects in Supercapacitors, Springer, Cham, Switzerland, 2015.

[35] A. Lewandowski, A. Olejniczak, M. Galinski, I. Stepniak, "Performance of carbon–carbon supercapacitors based on organic, aqueous and ionic liquid electrolytes", J. Power Sources 195 (17) (2010) 5814–5819.

[36] M.V. Fedorov, A.A. Kornyshev, Ionic liquids at electrified interfaces, Chem. Rev. 114 (5) (2014) 2978–3036.

[37] A. Balducci, F. Soavi, M. Mastragostino, The use of ionic liquids as solvent-free green electrolytes for hybrid supercapacitors, Appl. Phys. A 82 (4) (2006) 627–632.

[38] C. Arbizzani, G. Gabrielli, M. Mastragostino, Thermal stability and flammability of electrolytes for lithium-ion batteries, J. Power Sources 196 (10) (2011) 4801–4805.

[39] J. Reiter, S. Jeremias, E. Paillard, M. Winter, S. Passerini, Fluorosulfonyl-(trifluoromethanesulfonyl)imide ionic liquids with enhanced asymmetry, Phys. Chem. Chem. Phys. 15 (7) (2013) 2565–2571.

[40] S. Jeremias, M. Kunze, S. Passerini, M. Schonhoff, Polymerizable ionic liquid with state of the art transport properties, J. Phys. Chem. B 117 (36) (2013) 10596–10602.

[41] K. Hayamizu, Y. Aihara, H. Nakagawa, T. Nukuda, W.S. Price, Ionic conduction and ion diffusion in binary room-temperature ionic liquids composed of [emim][BF4] and LiBF4, J. Phys. Chem. B 108 (50) (2004) 19527–19532.

[42] D. Dunn, J. Newman, Predictions of specific energies and specific powers of double-layer capacitors using a simplified model, J. Electrochem. Soc. 147 (3) (2000) 820–830.

[43] O. Bohlen, J. Kowal, D.U. Sauer, Ageing behaviour of electrochemical double layer capacitors: Part II. lifetime simulation model for dynamic applications, J. Power Sources 173 (1) (2007) 626–632.

[44] Y. Dandeville, P. Guillemet, Y. Scudeller, O. Crosnier, L. Athouel, T. Brousse, Measuring time-dependent heat profiles of aqueous electrochemical capacitors under cycling, Thermochim. Acta 526 (1–2) (2011) 1–8.

[45] A.L. d'Entremont, L. Pilon, First-order thermal model of commercial EDLCs, Appl. Therm. Eng. 67 (12) (2014) 439–446.

[46] A.L. d'Entremont, L. Pilon, First-principles thermal modeling of electric double layer capacitors under constant-current cycling, J. Power Sources 246 (2014) 887–898.

[47] A.L. d'Entremont, L. Pilon, Thermal effects of asymmetric electrolytes in electric double layer capacitors, J. Power Sources 273 (2015) 196–209.

[48] O. Munteshari, J. Lau, A. Krishnan, B. Dunn, L. Pilon, Isothermal calorimeter for measurements of time-dependent heat generation rate in individual supercapacitor electrodes, J. Power Sources 374 (2018) 257–268.

[49] C. Arbizzani, M. Biso, D. Cericola, M. Lazzari, F. Soavi, M. Mastragostino, Safe, high-energy supercapacitors based on solvent-free ionic liquid electrolytes, J. Power Sources 185 (2) (2008) 1575–1579.

[50] S. Pohlmann, T. Olyschläger, P. Goodrich, J.A. Vicente, J. Jacquemin, A. Balducci, Azepanium-based ionic liquids as green electrolytes for high voltage supercapacitors, J. Power Sources 273 (2015) 931–936.

[51] A. Balducci, W.A. Henderson, M. Mastragostino, S. Passerini, P. Simon, F. Soavi, Cycling stability of a hybrid activated carbon//poly (3-methylthiophene) supercapacitor with N-butyl-N-methylpyrrolidinium bis(trifluoromethanesulfonyl)imide ionic liquid as electrolyte, Electrochim. Acta 50 (11) (2005) 2233–2237.

[52] S. Zhang, S. Brahim, S. Maat, High-voltage operation of binder-free CNT supercapacitors using ionic liquid electrolytes, J. Mater. Res. 33 (9) (2018) 1179–1188.

[53] M. Nádherná, J. Reiter, J. Moškon, R. Dominko, "Lithium bis (fluorosulfonyl) imide–PYR14 TFSI ionic liquid electrolyte compatible with graphite", J. Power Sources 196 (18) (2011) 7700–7706.

[54] A. Brandt, A. Balducci, Theoretical and practical energy limitations of organic and ionic liquid-based electrolytes for high voltage electrochemical double layer capacitors, J. Power Sources 250 (2014) 343–351.

[55] F. Soavi, C. Arbizzani, M. Mastragostino, Leakage currents and self-discharge of ionic liquid-based supercapacitors, J. Appl. Electrochem. 44 (4) (2014) 491–496.

[56] P. Johansson, L.E. Fast, A. Matic, G.B. Appetecchi, S. Passerini, The conductivity

of pyrrolidinium and sulfonylimide-based ionic liquids: a combined experimental and computational study, J. Power Sources 195 (7) (2010) 2074−2076.

[57] A. Balducci, R. Dugas, P.-L. Taberna, P. Simon, D. Plee, M. Mastragostino, S. Passerini, "High temperature carbon−carbon supercapacitor using ionic liquid as electrolyte", J. Power Sources 165 (2) (2007) 922−927.

[58] S. Leyva-García, D. Lozano-Castelló, E. Morallón, T. Vogl, C. Schütter, S. Passerini, A. Balducci, D. Cazorla-Amorós, Electrochemical performance of a superporous activated carbon in ionic liquid-based electrolytes, J. Power Sources 336 (2016) 419−426.

[59] M. Arulepp, L. Permann, J. Leis, A. Perkson, K. Rumma, A. Jänes, E. Lust, Influence of the solvent properties on the characteristics of a double layer capacitor, J. Power Sources 133 (2) (2004) 320−328.

[60] A. Hammar, P. Venet, R. Lallemand, G. Coquery, G. Rojat, Study of accelerated aging of supercapacitors for transport applications, IEEE Trans. Ind. Electron. 57 (12) (2010) 3972−3979.

[61] P. Kreczanik, P. Venet, A. Hijazi, G. Clerc, Study of supercapacitor aging and lifetime estimation according to voltage, temperature, and RMS current, IEEE Trans. Ind. Electron. 61 (9) (2014) 4895−4902.

[62] P. Liu, M. Verbrugge, S. Soukiazian, Influence of temperature and electrolyte on the performance of activated-carbon supercapacitors, J. Power Sources 156 (2) (2006) 712−718.

[63] W. Liu, X. Yan, J. Lang, Q. Xue, Effects of concentration and temperature of EMIMBF$_4$/acetonitrile electrolyte on the supercapacitive behavior of graphene nanosheets, J. Mater. Chem. 22 (18) (2012) 8853−8861.

[64] W. Li, K. Xu, L. An, F. Jiang, X. Zhou, J. Yang, Z. Chen, R. Zou, J. Hu, Effect of temperature on the performance of ultrafine MnO$_2$ nanobelt supercapacitors, J. Mater. Chem. 2 (5) (2014) 1443−1447.

[65] J.-G. Wang, Y. Yang, Z.-H. Huang, F. Kang, Effect of temperature on the pseudo-capacitive behavior of freestanding MnO$_2$@ carbon nanofibers composites electrodes in mild electrolyte, J. Power Sources 224 (2013) 86−92.

[66] C. Yuan, X. Zhang, Q. Wu, B. Gao, Effect of temperature on the hybrid supercapacitor based on NiO and activated carbon with alkaline polymer gel electrolyte, Solid State Ionics 177 (13) (2006) 1237−1242.

[67] S. Park, S.-W. Kang, K. Kim, Competition between ionic adsorption and desorption on electrochemical double layer capacitor electrodes in acetonitrile solutions at different currents and temperatures, J. Power Sources 372 (2017) 8−15.

[68] B. Xu, F. Wu, R. Chen, G. Cao, S. Chen, Y. Yang, Mesoporous activated carbon fiber as electrode material for high-performance electrochemical double layer capacitors with ionic liquid electrolyte, J. Power Sources 195 (7) (2010) 2118−2124.

[69] M. Ayadi, A. Eddahech, O. Briat, J.-M. Vinassa, Voltage and temperature impacts on leakage current in calendar ageing of supercapacitors, in: Proceedings of the 4th International Conference on Power Engineering, Energy and Electrical Drives, IEEE, 2013, pp. 1466−1470.

[70] T. Umemura, Y. Mizutani, T. Okamoto, T. Taguchi, K. Nakajima, K. Tanaka, Life expectancy and degradation behavior of electric double layer capacitor part I, in: Proceedings of the 7th International Conference on Properties and Applications of Dielectric Materials, vol. 3, IEEE, 2003, pp. 944−948.

[71] M. Hahn, R. Kötz, R. Gallay, A. Siggel, Pressure evolution in propylene carbonate based electrochemical double layer capacitors, Electrochim. Acta 52 (4) (2006) 1709−1712.

[72] A.M. Bittner, M. Zhu, Y. Yang, H.F. Waibel, M. Konuma, U. Starke, C.J. Weber, Ageing of electrochemical double layer capacitors, J. Power Sources 203 (2012) 262−273.

[73] O. Munteshari, J. Lau, D.S. Ashby, B. Dunn, L. Pilon, Effects of constituent materials on heat generation in individual EDLC electrodes, J. Electrochem. Soc. 165 (7) (2018) A1547−A1557.

[74] M.Z. Bazant, B.D. Storey, A.A. Kornyshev, Double layer in ionic liquids: overscreening versus crowding, Phys. Rev. Lett. 106 (4) (2011), 046102.

[75] M.D. Levi, N. Levy, S. Sigalov, G. Salitra, D. Aurbach, J. Maier, Electrochemical quartz crystal microbalance (EQCM) studies of ions and solvents insertion into highly porous activated carbons, J. Am. Chem. Soc. 132 (38) (2010) 13220−13222.

[76] J. Chmiola, C. Largeot, P.-L. Taberna, P. Simon, Y. Gogotsi, Desolvation of ions in subnanometer pores and its effect on capacitance and double-layer theory,

[77] B. Wilson, R. Georgiadis, J.E. Bartmess, Enthalpies of solvation of ions. Aliphatic carboxylic acids: steric hindrance to solvation, J. Am. Chem. Soc. 113 (5) (1991) 1762−1766.

[78] P.J. Beach, Heats of Solvation of Organic Liquids in Room Temperature Ionic Liquids, Master's thesis, University of Tennessee - Knoxville, 2008.

[79] S. Pohlmann, T. Olyschläger, P. Goodrich, J.A. Vicente, J. Jacquemin, A. Balducci, Mixtures of azepanium based ionic liquids and propylene carbonate as high voltage electrolytes for supercapacitors, Electrochim. Acta 153 (2015) 426−432.

[80] H. Wang, L. Pilon, "Reply to comments on "Intrinsic limitations of impedance measurements in determining electric double layer capacitances"by H. Wang and L. Pilon [Electrochimica Acta 63 (2012) 55]", Electrochim. Acta 76 (2012) 529−531.

[81] A. Borenstein, R. Attias, O. Hanna, S. Luski, R.B. Kaner, D. Aurbach, A surprising failure mechanism in symmetric supercapacitors at high voltages, ChemElectroChem 4 (10) (2017) 2660−2668.

[82] A. Burke, M. Miller, Testing of electrochemical capacitors: capacitance, resistance, energy density, and power capability, Electrochim. Acta 55 (25) (2010) 7538−7548.

[83] S. Zhao, F. Wu, L. Yang, L. Gao, A.F. Burke, A measurement method for determination of DC internal resistance of batteries and supercapacitors, Electrochem. Commun. 12 (2) (2010) 242−245.

[84] M.D. Stoller, R.S. Ruoff, "Best practice methods for determining an electrode material's performance for ultracapacitors", Energy Environ. Sci. 3 (9) (2010) 1294−1301.

[85] B.-A. Mei, O. Munteshari, J. Lau, B. Dunn, L. Pilon, Physical interpretations of Nyquist plots for EDLC electrodes and devices, J. Phys. Chem. C 122 (1) (2017) 194−206.

[86] S.R.C. Vivekchand, C.S. Rout, K.S. Subrahmanyam, A. Govindaraj, C.N.R. Rao, Graphene-based electrochemical supercapacitors, J. Chem. Sci. 120 (1) (2008) 9−13.

[87] V.L. Martins, A.J.R. Rennie, N. Sanchez-Ramirez, R.M. Torresi, P.J. Hall, Improved performance of ionic liquid supercapacitors by using tetracyano-borate anions, ChemElectroChem 5 (4) (2018) 598−604.

[88] A.J.R. Rennie, V.L. Martins, R.M. Smith, P.J. Hall, Influence of particle size distribution on the performance of ionic liquid-based electrochemical double layer capacitors, Sci. Rep. 6 (2016) 22062.

[89] C. Kim, Electrochemical characterization of electrospun activated carbon nanofibres as an electrode in supercapacitors, J. Power Sources 142 (1−2) (2005) 382−388.

[90] Y. Gao, Y.S. Zhou, M. Qian, X.N. He, J. Redepenning, P. Goodman, H.M. Li, L. Jiang, Y.F. Lu, Chemical activation of carbon nano-onions for high-rate supercapacitor electrodes, Carbon 51 (2013) 52−58.

[91] H. Wang, L. Pilon, Physical interpretation of cyclic voltammetry for measuring electric double layer capacitances, Electrochim. Acta 64 (2012) 130−139.

[92] A. Likitchatchawankun, A. Kundu, O. Munteshari, T.S. Fisher, L. Pilon, Heat generation in all-solid-state supercapacitors with graphene electrodes and gel electrolytes, Electrochim. Acta 303 (2019) 341−353.

[93] E. Frackowiak, G. Lota, J. Pernak, Room-temperature phosphonium ionic liquids for supercapacitor application, Appl. Phys. Lett. 86 (16) (2005) 164104.

[94] D. Wei, T.W. Ng, Application of novel room temperature ionic liquids in flexible supercapacitors, Electrochem. Commun. 11 (10) (2009) 1996−1999.

[95] S. Pohlmann, R.-S. Kühnel, T.A. Centeno, A. Balducci, "The influence of anion−cation combinations on the physicochemical properties of advanced electrolytes for supercapacitors and the capacitance of activated carbons", ChemElectroChem 1 (8) (2014) 1301−1311.

[96] D.R. MacFarlane, M. Forsyth, E.I. Izgorodina, A.P. Abbott, G. Annat, K. Fraser, On the concept of ionicity in ionic liquids, Phys. Chem. Chem. Phys. 11 (25) (2009) 4962−4967.

[97] K. Hayamizu, Y. Aihara, S. Arai, C.G. Martinez, Pulse-gradient spin-echo 1H, 7Li, and 19F NMR diffusion and ionic conductivity measurements of 14 organic electrolytes containing LiN(SO$_2$CF$_3$)$_2$, J. Phys. Chem. B 103 (3) (1999) 519−524.

[98] K. Dixler, W. Kwok, Active and passive cooling for an energy storage module, 2014, p. 573. U.S. Patent App. 13/710.